EARLY CAREER SCHOLARS IN MATERIALS SCIENCE 2023

Resolving intragranular stress fields in plastically deformed titanium using point-focused high-energy diffraction microscopy

Wenxi Li[1,2], Hemant Sharma[3], Peter Kenesei[3], Sidharth Ravi[4], Huseyin Sehitoglu[4], Ashley Bucsek[1,2,a]

[1] Department of Mechanical Engineering, University of Michigan, 2350 Hayward St, Ann Arbor, MI 48109, USA
[2] Department of Materials Science and Engineering, University of Michigan, 2300 Hayward St, Ann Arbor, MI 48109, USA
[3] X-Ray Science Division, Argonne National Laboratory, 9700 S Cass Avenue, Lemont, IL 60439, USA
[4] Department of Mechanical Science and Engineering, University of Illinois at Urbana-Champaign, 105 S. Mathews Ave, Urbana, IL 61801, USA
[a] Address all correspondence to this author. e-mail: abucsek@umich.edu

The response of a polycrystalline material to a mechanical load depends not only on the response of each individual grain, but also on the interaction with its neighbors. These interactions lead to local, intragranular stress concentrations that often dictate the initiation of plastic deformation and consequently the macroscopic stress–strain behavior. However, very few experimental studies have quantified intragranular stresses across bulk, three-dimensional volumes. In this work, a synchrotron X-ray diffraction technique called point-focused high-energy diffraction microscopy (pf-HEDM) is used to characterize intragranular deformation across a bulk, plastically deformed, polycrystalline titanium specimen. The results reveal the heterogenous stress distributions within individual grains and across grain boundaries, a stress concentration between a low and high Schmid factor grain pair, and a stress gradient near an extension twinning boundary. This work demonstrates the potential for the future use of pf-HEDM for understanding the local deformation associated with networks of grains and informing mesoscale models.

Ashley Bucsek is an Assistant Professor of Mechanical Engineering at the University of Michigan since 2019 with a courtesy appointment in Materials Science and Engineering. Previously, she was a President's Postdoctoral Fellow at the University of Minnesota, a visiting scientist on beamline ID06 at the European Synchrotron Radiation Facility, and a National Science Foundation (NSF) Graduate Research Fellow at Colorado School of Mines where she received her PhD and Master's in Mechanical Engineering. Her research combines cutting-edge in-situ X-ray diffraction microscopy techniques with micromechanical theory to study microscale deformation and microstructure evolution in structural and functional materials. She is the President of the Board of Directors for the ASM International Organization for Shape Memory and Superelastic Technologies, an Advanced Photon Source (APS) Imaging/Microbeam Proposal Review Panel member, an APS Users' Organization Steering Committee member, a Cornell High Energy Synchrotron Source (CHESS) User Executive Committee Member, and the Community Development Officer for the International Union of Crystallography Commission on Diffraction Microstructure Imaging. Her research is funded under the Department of Energy Basic Energy Sciences. She is a 2022 NSF CAREER award recipient and a 2023 Air Force Office of Scientific Research (AFOSR) Young Investigator Program (YIP) recipient.

Ashley Bucsek

Introduction

The vast majority of engineering materials are polycrystalline: a network of distinctly oriented crystals, or grains. Understanding how elastic and plastic deformation initiates and propagates through this network is the key to predicting polycrystalline material behavior, preventing catastrophic failure, and developing novel engineering materials with improved performance [1–7]. However, the connectivity of the grain network causes local, intragranular stress variations that can deviate from the average (macroscopic) stress response drastically, and many active areas of research are directed toward both predicting these variations and understanding the consequences on plastic deformation [8–13], damage [14–18], and crack initiation [16, 18–21].

For example, one well-known consequence of intragranular stress variations is non-Schmid behavior. Non-Schmid behavior is observed in all polycrystalline materials but particularly in materials with hexagonal close-packed (hcp) structures like α titanium (Ti). The activation of both plastic slip and deformation twinning is predicted using a critical resolved shear stress (CRSS) criterion that states that a specific plastic deformation mode will initiate when its unique CRSS value is exceeded: This is known as Schmid's law. For hcp materials, reports showing a breakdown of Schmid's law called non-Schmid behavior are prolific (e.g., [22–41]), with potentially both atomic-scale and microscale origins. At the atomic scale, conventional Schmid's law does not account for sensitivities to the full 3D stress state (i.e., beyond the RSS) in cases where non-glide stress components influence non-planar dislocation core structures. At the microscale, grain neighborhood interactions can lead to intragranular stress concentrations, but without the ability to resolve these local stress states, the correct stress to Schmid's law cannot be inputted thus leading to the appearance of non-Schmid-type behavior. To study and de-couple atomic-scale and microscale origins of non-Schmid observations, we need local measurements of the full 3D stress state across statistically significant volumes. A slightly different but related example of a critical need for intragranular stress measurements is the study of grain boundaries and the initiation, transfer, and impedance of plastic deformation. The behavior of plastic deformation at and across grain boundaries is related to defect accumulation, stress concentrations, and orientation relationships, also becoming preferential sites for damage and failure nucleation [42–49]. As a result, the direct experiment observation of the complex stress evolution at and across grain boundaries is of great interest to the material science community [18, 50–56].

Over the past two decades, high-energy diffraction microscopy (HEDM) [57], which falls under the umbrella of three-dimensional X-ray diffraction (3DXRD) [58–60] techniques wherein the sample is illuminated by high-energy monochromatic synchrotron X-rays during a 360° sample rotation, has opened new doors for resolving the microstructural and mechanical evolution of polycrystalline materials. When the detector is placed far (~ 1 m) from the sample, classified as far-field HEDM (ff-HEDM) [61, 62], the elastic strain tensor, crystallographic orientation, location, and relative volume of each individual grain can be measured for tens of thousands of grains per scan [63]. However, with ff-HEDM, these values are averaged over each grain, i.e., grain-averaged. When a high-resolution detector is placed near (~10 mm) the sample, classified as near-field HEDM (nf-HEDM), the crystallographic orientation can be spatially resolved (e.g., [64, 65]) revealing the morphology and connectivity of the grain network. However, with nf-HEDM, the elastic strain tensor cannot be easily measured (although exciting progress has been made toward these efforts recently [66, 67]). The ff-HEDM orientation, spatial, and strain resolutions are approximately 0.02°, 5 μm, and 2×10^{-4}, respectively [68], and the nf-HEDM orientation and spatial resolution are approximately 0.1° and $1 - 2$ μm, respectively [6, 69, 70]. Ff-HEDM and nf-HEDM are performed using a "box" beam [16, 62, 71, 72] or a vertically focused "line" beam [62, 64, 65] wherein the entire width of the cross-section of a sample is illuminated.

The newest variation of HEDM, which we refer to here as point-focused HEDM (pf-HEDM), is capable of both intragranular orientation and intragranular elastic strain tensor measurements, combining the collective advantages of nf-HEDM and ff-HEDM with up to $100 \times$ increases in spatial resolution (from tens of micrometers to hundreds of nanometers depending on available beam focusing capabilities). With pf-HEDM, a horizontally and vertically focused ("pencil") beam is rastered across the sample, recording ff-HEDM measurements at each raster location. Whereas ff-HEDM measurements are averaged over each grain, pf-HEDM measurements are averaged over the incident beam. Thus, if the beam size is smaller than the grain size, then ff-HEDM information (elastic strain tensor and crystallographic orientation) can be reconstructed intragranularly. In this way, pf-HEDM provides high-resolution spatially resolved measurements of orientation and elastic strain information similar to Bragg coherent diffraction imaging (BCDI) [73–76], dark-field X-ray microscopy (DFXM) [77–80], or differential-aperture X-ray microscopy (DAXM) [81–83]. The main differences between these other high-resolution techniques and pf-HEDM are that pf-HEDM measurements can be made across mm-sized networks of differently oriented grains with ease (i.e., without requiring any grain alignment or custom sample tilting), and pf-HEDM is not limited by sample tilting/rocking capabilities to capture potentially large intragranular orientation/strain gradients.

To our knowledge, pf-HEDM has been demonstrated by only two groups since 2019, both of which refer to it as scanning

3DXRD. (3DXRD is the preferred terminology outside of the U.S., while HEDM is the preferred terminology within the U.S. The International Union of Crystallography (IUCr) commission on Diffraction Microstructure Imaging (DMI) has current efforts to resolve these differences in taxonomy, the results of which are expected to be published in the near future.) In the first demonstration of scanning 3DXRD, Hayashi et al. measured the evolution of intragranular stresses in a low-carbon steel that undergone 5.1% elongation during tensile loading with 2.4 μm spatial resolution [84]. Later, Hektor et al. and Henningsson et al. used scanning 3DXRD to study local stress variations during grain growth around a tin whisker with 250 nm spatial resolution [85, 86].

To retrieve the high fidelity of intragranular orientation and strain variations, important notable efforts have been made by these groups. Initially, Hayashi et al. proposed a per-voxel refinement method to approximate the orientation and strain using scanning 3DXRD data [84, 87–89]. The orientation and strain at each voxel within a grain were approximated independently by fitting the orientation and lattice parameters to the subset of diffraction peaks that intersected the voxel. Then, the grain morphology was determined by the discontinuity of orientation across a boundary based on the obtained orientation map. The primary assumption involved in this approach is that the subset of diffraction peaks intersected through a voxel *only* emanated from that single voxel, not from the entire region illuminated by the beam through the grain (and other grains). As a result, this method was shown to introduce bias and underestimate the strain gradient during strain reconstruction by Henningsson et al. [86]. Henningsson et al. [86] proposed a polycrystal refinement method that used prior knowledge of grain morphology obtained using a filtered back-projection algorithm before the intragranular orientation and strain reconstruction. Then, the connected grain map was obtained by superposing the boundaries of individual grains. The intragranular variation across the grain was retrieved by fitting the orientation and strain of *all* voxels inside a grain intersected by the beam simultaneously. To improve computational efficiency, an algebraic strain refinement method that added smooth constraints to suppress the high-frequency variation in strain components during the strain refinement process was proposed in the same work. More recently, Henningsson et al. [90] adopted a Gaussian process framework to incorporate a static equilibrium constraint during the local strain refinement and provided an uncertainty estimation in the reconstructed strain field. Only intragranular strain reconstruction results have been shown in Henningsson and Hektor's work (i.e., without reconstructing the intragranular misorientation).

The pf-HEDM intragranular orientation and strain reconstruction quality strongly depends on the peak searching and peak indexing capabilities of the chosen analysis software.

Peak searching refers to the process of identifying individual Bragg reflections in the thresholded and background-subtracted pf-HEDM images. Peak indexing refers to the process of determining each grain orientation, strain, and centroid by sorting the scattering vectors converted from peak searching. Multiple open-source software packages exist for ff-HEDM, including FABLE [91–93], HEXRD [61], and MIDAS [94, 95], and these packages can be adapted and used for pf-HEDM data analysis. The peak searching and indexing process in Hayashi et al. and Henningsson et al.'s work was performed using the main software package in FABLE, ImageD11 (https://github.com/FABLE-3DXRD/ImageD11). When the peaks can be unambiguously separated and determined during the peak searching process, then the indexing process can be readily implemented. However, when the peaks overlap due to plastic deformation or the number of simultaneously illuminated grains being large, additional approaches, including volume reduction method [10] or the use of a conical slit [84, 96, 97], have to be adopted. Moreover, the resolution of grain boundaries resolved by filtered back-projection will deteriorate [98], due to its sensitivity to diffraction peak intensity and indexing accuracy.

The pf-HEDM work presented in this manuscript uses advancements implemented in MIDAS [94, 95], namely, a multi-peak fitting approach and surface-scanning method designed to improve the peak indexing even in the case of overlapping or plastically deformed Bragg peaks. In this work, we present the results of a pf-HEDM experiment on a plastically deformed commercially pure (CP) hcp α-Ti specimen that was strained to 7% under uniaxial tension with a residual plastic strain of ~ 6.5%. A new framework for reconstructing pf-HEDM datasets is used that is now available within MIDAS. Instead of using the filtered back-projection algorithm, each grain is reconstructed based on the obtained orientation map at each voxel without prior knowledge. The advantage of this algorithm is the ability to yield more accurate information at the grain boundaries, down to one voxel, even under significant sample deformation and diffraction peak overlap. The intragranular orientation and strain at each voxel are then refined and optimized using a gradient descent algorithm [99] by taking into account all voxels within the grain intersected by the beam simultaneously. (The details associated with this new analysis are discussed more in the section titled "Pf-HEDM analysis" and are the subject of an upcoming paper by Sharma et al.) The results show both the intragranular orientation and the local stress field across individual grains and grain boundaries. Pf-HEDM reconstruction results are compared against those measured using ff-HEDM and nf-HEDM and match well with grain-averaged orientation and strain results. Finally, a stress concentration between a low and high Schmid factor grain pair and a stress gradient near an extension twinning
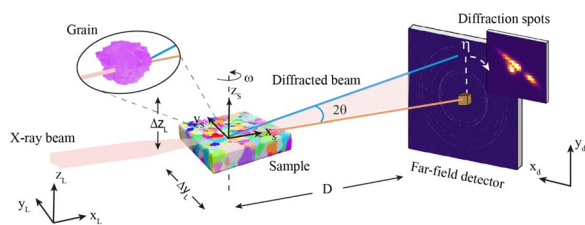
Figure 1: Schematic of the pf-HEDM setup at the APS 1-ID-E beamline. The subscripts L, S, and d refer to the laboratory, sample, and detector coordinate systems, respectively. The diffraction angle 2θ, sample rotation angle ω, and azimuthal angle η are shown.

boundary are observed and discussed. These results demonstrate the potential for future cross-cutting opportunities for using pf-HEDM to understand the local elastic and plastic deformation associated with networks of grains in polycrystalline materials.

Ff-HEDM and nf-HEDM measurements

The HEDM experiments were conducted at beamline 1-lD-E at the advanced photon source (APS). A monolithic Si (111) bent double-Laue crystal monochromator was used on the synchrotron radiation of a superconducting undulator source at 55.67 keV with 0.001 relative energy bandwidth (ΔE/E) [100]. Prior to the HEDM experiment, LaB6 standard powder was used to calibrate the detector parameters (sample-to-detector distance, detector tilt angles, and detector distortion) of the far-field detector. And Au standard was used to get an initial guess of the sample-to-detector distance at each position for the near-field detector. The exact position was calibrated using the Ti sample. For the ff-HEDM measurements, a 1.7 mm (width) × 0.2 mm (height) beam was used to characterize the volume of interest. The far-field detector consisted of a single amorphous silicon flat-panel GE detector [101] (2048 × 2048 pixels) with a pixel size of 200 μm, placed at a distance of 0.968 m from the sample. Diffraction patterns were integrated over 0.25° rotation increments with an exposure time of 0.02 s as the sample rotated 360° about the vertical axis (z_S) as shown in Fig. 1, which coincided with the original loading direction of the sample. A total of 1440 diffraction images were collected per measurement. Including the time for the detectors to output the data, each ff-HEDM measurement took roughly 6 min. For the nf-HEDM measurements, the near-field detector consisted of a LuAG:Ce 25 μm-thick single-crystal scintillator and 2048 × 2048 CCD camera (QImaging Retiga 4000DC, using a Kodak KAI-4022 CCD chip) with a 5 × Mitutoyo long working distance optical objective lens; the camera has 1.48 μm effective pixel pitch. Nf-HEDM measurements were taken with the near-field detector placed nominally at 5 and 7 mm from the sample. For each nf-HEDM measurement, a line-focused beam of 1.7 mm (width) × 1 μm

(height) X-ray was used, and five sets of measurements were taken at a vertical separation distance of 10 μm. Diffraction patterns were integrated over every 0.25° interval as the sample was rotated 360° resulting in a total of 1440 diffraction images per scan. The exposure time for each image was 1.5 s for a total of ~ 35 min per layer. All ff-HEDM and nf-HEDM analyses were performed using MIDAS.

Pf-HEDM measurements

The pf-HEDM experiment setup is shown in Fig. 1. To acquire the information on the intragranular length scale, the incident X-ray beam should only illuminate part of the grain. Therefore, for the pf-HEDM measurements, the incident beam is focused horizontally and vertically to a size of 15 μm (horizontal) × 2 μm (vertical), which is smaller than the average grain size of the sample, using a pair of silicon compound refractive lenses [102]. During the pf-HEDM data acquisition process, the polycrystalline specimen is mounted on a turntable with a single rotation axis z_S and is free to move along the transverse beam directions y_L and z_L by the translational stage. The lab Cartesian coordinate system (x_L, y_L, z_L) is introduced to serve as a fixed point in all the measurements. The direction x_L is made to parallel to incident X-ray beam direction. The sample coordinate system (x_S, y_S, z_S) is introduced to extract the subset of the diffraction peaks at a voxel that is intersected by the X-ray ("Pf-HEDM analysis"). The turntable which holds the sample is translated across the X-ray beam with a step size to collect diffraction data from the volume of interest. Therefore, the rotation axis z_S is given a new position in the laboratory coordinate system. In this paper, for a given vertical position z_L, 105 rotation axis positions with a spacing of 15 μm were required to scan the entire sample cross-section. The scan step size along the y_L direction was equal to the horizontal X-ray beam size. At each rotation axis position, diffraction spots from Ti sample were recorded using a far-field detector while sample was rotated around z_S axis through an ω angle of 360° Each measurement was taken using the same rotation increment and detector distance as far-field HEDM discussed in "Ff-HEDM and nf-HEDM measurements." After the entire cross-section was scanned by the point-focused beam, the sample was then moved to the next vertical position z_L and the procedure was repeated until the sample was translated over a certain vertical range. In this paper, pf-HEDM measurement was performed at two vertical (z_L) positions separated by a vertical distance of 10 μm. These two measurements were centered at the center z_L position of the nf-HEDM and ff-HEDM measurements discussed in "Ff-HEDM and nf-HEDM measurements". Each pf-HEDM measurement took 9 h per vertical layer.

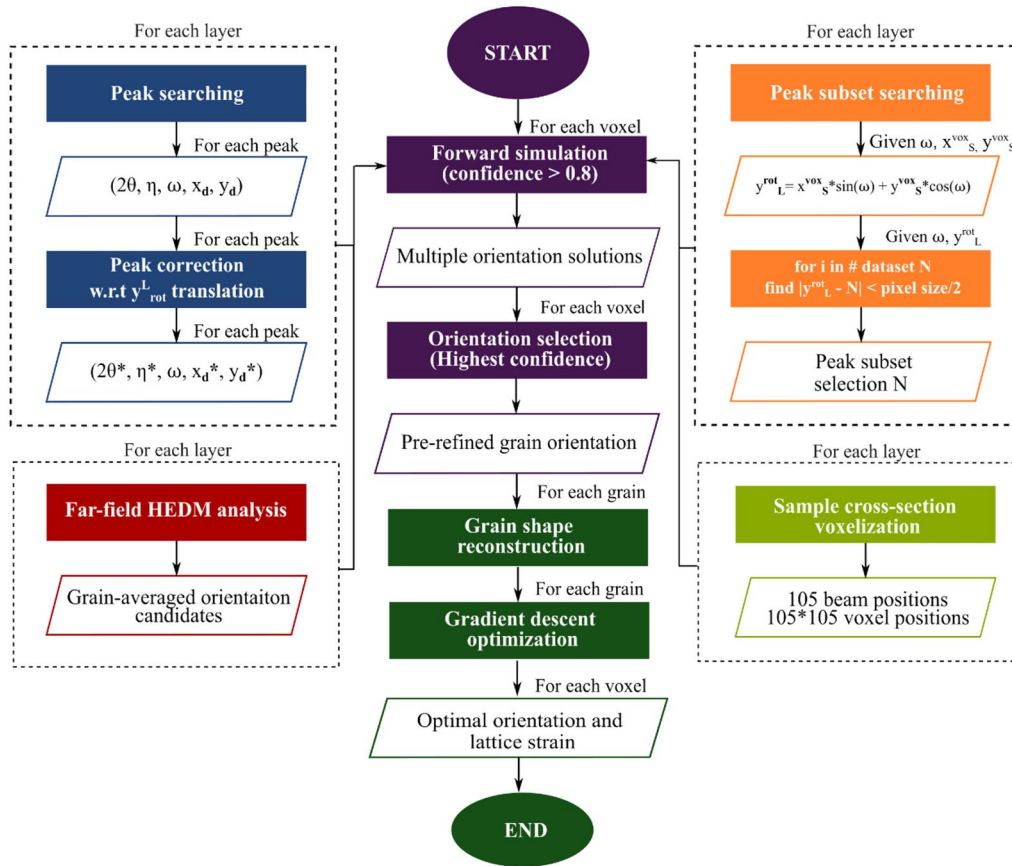## Pf-HEDM data reduction framework

Figure 2: Flowchart for the pf-HEDM data reduction procedure. Conventional ff-HEDM data processing steps are used in blue and red, and diffraction data subset selection and sample voxelization are performed in orange and light green. The new voxel-specific and resultant intragranular pf-HEDM processing steps are presented in purple and dark green, respectively.

Pf-HEDM analysis

In this paper, the proposed pf-HEDM data reduction framework is shown in Fig. 2. First, MIDAS begins with peak searching at each rotation axis position y^{rot}_L. The position of each peak is expressed in (x_d, y_d, ω) coordinates, where (x_d, y_d) is the detector pixel coordinate system and ω is the sample rotation angle. Each peak position can also be defined by the diffraction angle, azimuthal angle, and rotation angle $(2\theta, \eta, \omega)$ in the laboratory coordinate system as shown in Fig. 1. During the peak search process, a list of peaks, which is expressed in a five-dimensional vector $(2\theta, \eta, \omega, x_d, y_d)$, is identified and stored for each y^{rot}_L position. For bookkeeping purposes, the dataset number, N, is then labeled by the y^{rot}_L rotation axis position in the laboratory coordinate system. Since the rotation axis is translated along the positive y_L axis, the peak position needs to be corrected (i.e., translated in the negative y_L direction) with respect to the lab coordinate origin. Each peak is represented in a new five-dimensional vector $(2\theta^*, \eta^*, \omega, x_d^*, y_d^*)$ after this correction. Then, a list of orientation candidates

is independently generated by performing conventional ff-HEDM analysis. This step improves the computation efficiency. (Alternatively, MIDAS can also generate an exhaustive discretized set of candidate orientations based on the crystal structure and the full fundamental zone of corresponding orientation space.) A square voxel grid is then generated for the sample cross-section for individual voxel indexing and fitting. The size of the voxels corresponds to the beam size in the y_L direction (15 μm), so a total of 105×105 voxels are generated. Given a rotation angle ω and voxel position (x^{vox}_S, y^{vox}_S), we identify all of the y^{rot}_L rotation axis datasets that illuminated the corresponding voxel at some point during the sample rotation using Eq. (1). The subset of measured peaks that may potentially correspond to this voxel is then determined when the relative distance between rotation axis position y^{rot}_L and dataset number N, $|y^{rot}_L − N|$, is less than half of the voxel size. Then a forward simulation [64, 103, 104] is performed at each voxel using the list of orientation candidates from ff-HEDM analysis. The forward-modeled peaks are then compared with
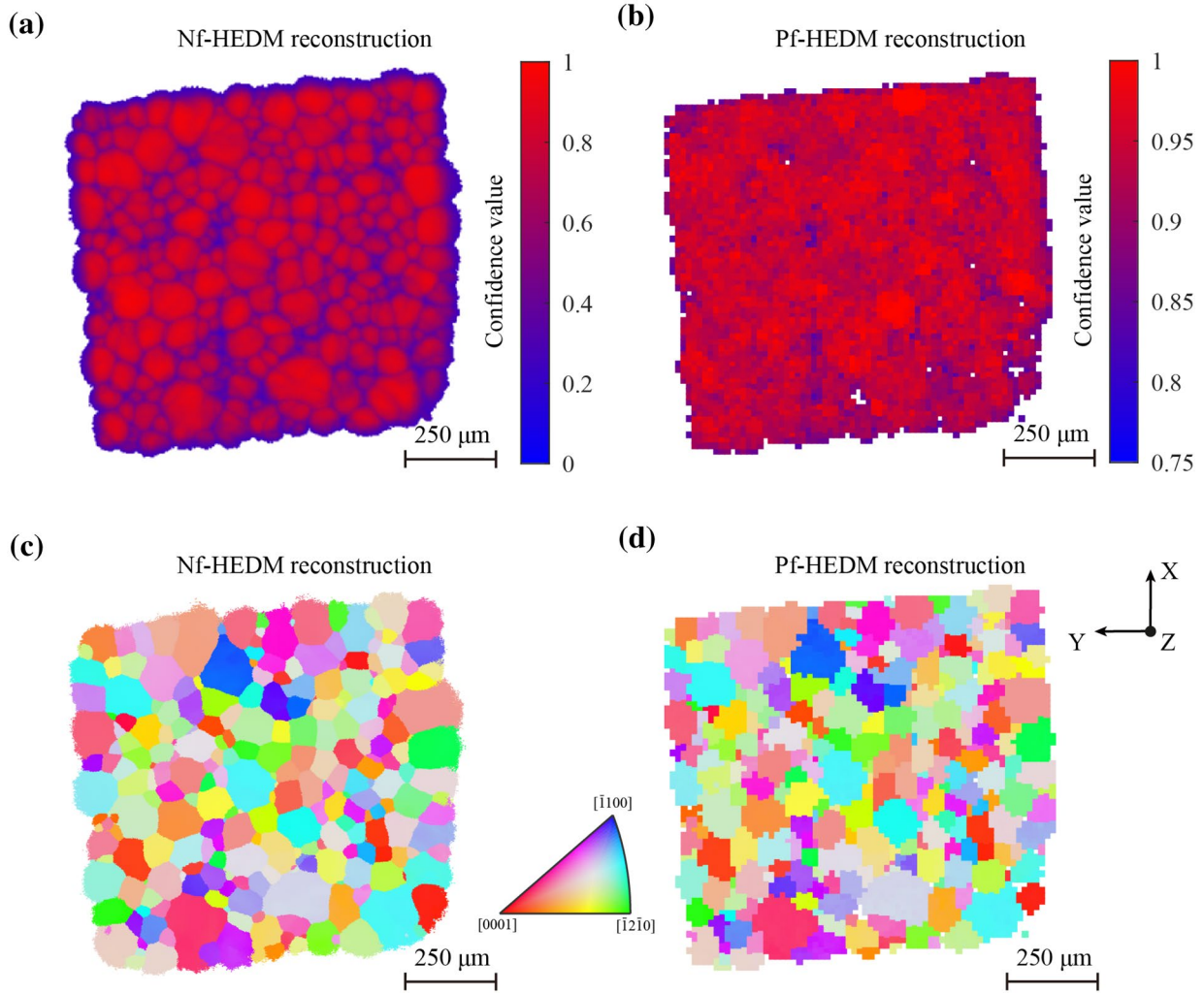
(a)

Nf-HEDM reconstruction

(b)

Pf-HEDM reconstruction

(c)

Nf-HEDM reconstruction

(d)

Pf-HEDM reconstruction

Figure 3: Comparison of nf-HEDM (a, c) versus pf-HEDM (b, d) reconstruction results: (a) and (b) shows the completeness of confidence value, (c) and (d) shows the spatially resolved crystallographic orientation maps where color corresponds to the inverse pole figure (IPF) shown which is normal to the vertical direction (z_L).

the measured diffraction data subset. The resulting orientations with a completeness value (the ratio of simulated diffraction peaks to the experimentally measured peaks) higher than a predefined threshold (we used 0.8) are stored for each voxel. This procedure can yield multiple solutions for each voxel, especially close to a grain boundary. The orientation with the highest confidence value is then assigned to each voxel, and the grain morphology and grain map is automatically determined

from the orientation map. A gradient descent algorithm [99] is used to optimize the forward simulation results of all voxels intersected by the beam with measured diffraction dataset. The intragranular orientation and lattice parameters are then refined and determined from this optimization.[1] The full details associated with this analysis procedure for pf-HEDM is the subject of an upcoming publication by Sharma et al.

$$y_L^{rot} = x_S^{vox} * \sin(\omega) + y_S^{vox} * \cos(\omega) \qquad (1)$$

Results

To verify the new pf-HEDM data reduction procedure, the pf-HEDM grain shape reconstruction results are compared with nf-HEDM in Figs. 3, 4, and the pf-HEDM strain mapping results are compared with the ff-HEDM results in Figs. 5, 7.
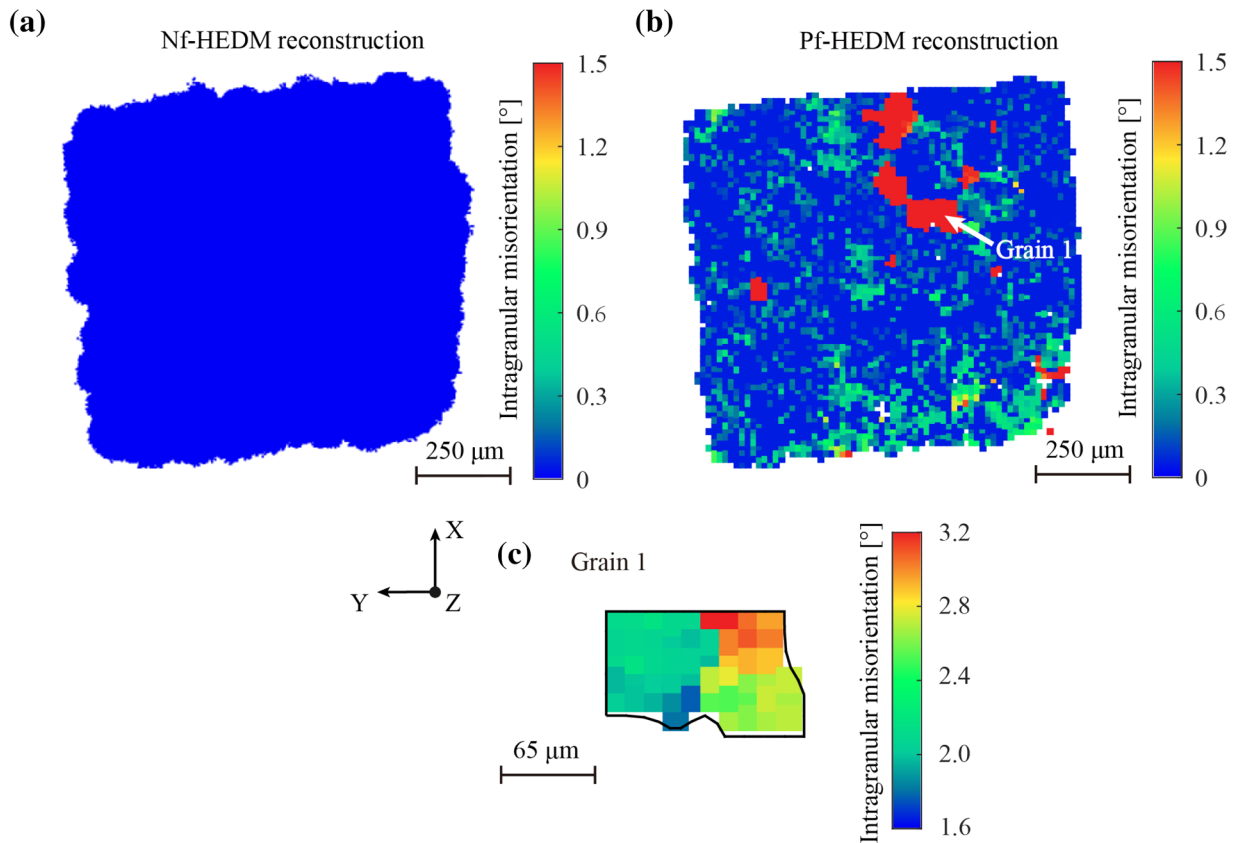
---

[1] In this paper, the average number of diffraction peaks is 168 per voxel. The maximum grain cross-section length is around 150 μm (10 voxels). For this largest grain, for example, the total number of unknowns is approximately 9*10*10 = 900 (where 9 is the number of unknown independent orientation and strain components), and the number of knowns is 168*10 = 1680 (where 168 is the number of peaks measured). Therefore, this system is overdetermined and the gradient descent algorithm can be applied to optimize the orientation (3 unknowns) and lattice parameter (6 unknowns) for each voxel.

(a) Nf-HEDM reconstruction

(b) Pf-HEDM reconstruction

(c) Grain 1

Figure 4: Comparison of nf-HEDM (a) versus pf-HEDM (b, c) reconstruction results: (a, b) spatially resolved intragranular misorientation maps; (c) intragranular misorientation map for the grain with the largest intragranular misorientation magnitude, labeled Grain 1.

Figure 3(a, b) shows the confidence map for nf-HEDM (left) versus pf-HEDM (right). As mentioned in "Pf-HEDM analysis," during the orientation indexing and optimization process, a forward simulation is performed in each voxel. A scalar metric, the completeness or confidence value, is assigned to each voxel, defined as the ratio of expected simulated peaks to the experimentally measured peaks. As is typical of conventional nf-HEDM reconstructions, in Fig. 3(a), the confidence value is high at the grain center and decreases as one approaches the grain boundaries. The disparity between confidence levels near to and far from the grain boundaries reveals the grain shapes. In contrast, the confidence value remains high throughout the pf-HEDM reconstruction in Fig. 3(b), even in pixels close to grain boundaries. The average confidence value is 0.93 with a minimum value of 0.8, meaning that, on average, 93% of the expected diffraction peaks are experimentally observed at each voxel. Figure 3(c, d) shows the spatially resolved crystallographic orientation at each voxel for conventional nf-HEDM (left) versus pf-HEDM (right). These visualizations were constructed using MTEX 5.8.1 [105]. Each grain and its neighbors can be distinguished by the discontinuity of orientation across the boundary. The nf-HEDM orientation map in Fig. 3(c)

matches well with the pf-HEDM orientation map in Fig. 3(d) with the only major difference being the spatial resolution, i.e., the 'irregular' grain shape in pf-HEDM is because the current spatial resolution of pf-HEDM is 15 μm instead of 2 μm in nf-HEDM.

Figure 4(a, b) shows intragranular misorientation maps of matched cross-sections in Fig. 3. Intragranular misorientation is defined here as the misorientation angle of each voxel inside a grain with respect to the grain mean orientation. As expected, intragranular misorientation is almost zero throughout the nf-HEDM map in Fig. 4(a), but the intragranular voxel orientations deviate from the mean grain orientations with a misorientation angle greater than 1.5° for pf-HEDM in Fig. 4(b). The grain with the largest intragranular misorientation angle magnitude is plotted in Fig. 4(c) with an expanded scale ranging from 1.6° to 3.2° to highlight the local intragranular variation.

Figure 5 shows the comparison between the results of the ff-HEDM analysis and the pf-HEDM analysis. Figure 5(a) show the ff-HEDM reconstruction where each grain is represented by a hexagonal prism. The location of each prism corresponds to the grain centroid position, the size of each prism corresponds to the relative grain volume, and the color of each prism
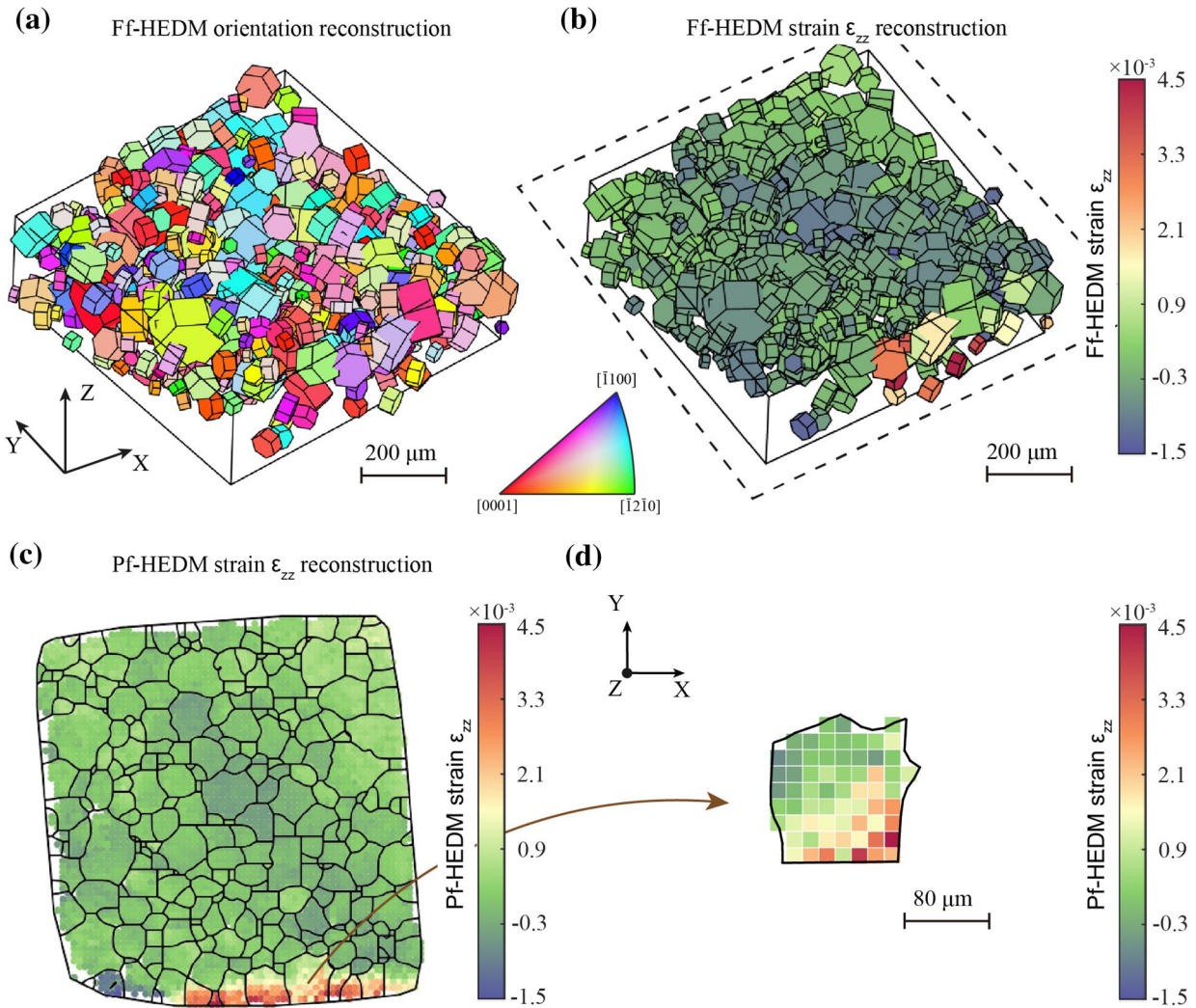
Figure 5: Comparison of ff-HEDM (a, b) versus pf-HEDM (c, d) reconstruction results: (a) ff-HEDM reconstruction where each grain is indicated by a hexagonal prism. The location of each prism corresponds to the grain centroid position, the size of each prism corresponds to the relative grain volume, and the color of each prism corresponds to the grain orientation according to the IPF shown on the right. (b) The same ff-HEDM reconstruction is shown in (a), except now the color of each prism corresponds to the grain-averaged elastic strain in the loading direction ε_{zz}. (c) pf-HEDM colored by the local elastic strain in the loading direction ε_{zz}. (d) Intragranular pf-HEDM elastic strain in the loading direction for one select grain from (c).

corresponds to the grain orientation according to the IPF. Figure 5(b) shows the grain-averaged elastic strain along loading direction, ε_{zz}, obtained from the ff-HEDM analysis. (Although we can measure the full elastic strain tensor, for simplicity, only strain component ε_{zz} is shown.) Several grains near the sample surface display a relatively higher grain-averaged elastic strain value due to the fact that this particular surface was polished. In comparison, Fig. 5(c) shows the local elastic strain values from the pf-HEDM analysis. Notice that the local strain values are nominally the same between the two analysis types, with the main difference being the higher spatial resolution of the pf-HEDM technique. Even the grains that exhibit high stress concentrations due to polishing are captured

in both Fig. 5(b) and (c), though in Fig. 5(c), we can resolve the depth of the polishing effects, which end about halfway through the surface grains and cause a noticeable gradient. The heterogeneous strain distribution within one select individual grain is shown in Fig. 5(d).

The stress tensor can be resolved by ff-HEDM and pf-HEDM from the measured elastic strain tensor using Hooke's law. To convert the measured elastic strain values to stress, we used the elastic constants for pure Ti ($C_{11} = 160$, $C_{12} = 90$, $C_{13} = 66$, $C_{33} = 181$, $C_{44} = 46.5$ GPa) [106]. The spatially resolved stress measured using pf-HEDM is shown in Fig. 6. Although we can measure the full stress tensor, for simplicity, only the stress in the original loading direction, σ_{zz}, is shown.
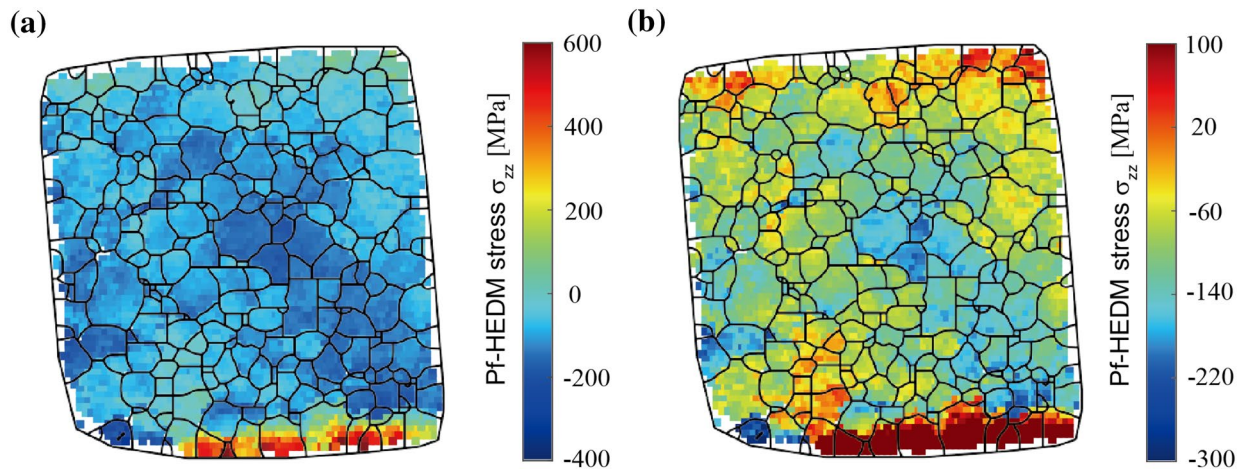
(a)

(b)

Figure 6: Pf-HEDM reconstruction of the stress along the loading direction σ_{zz}: (a) pf-HEDM reconstruction result with a large color bar range. (b) The same pf-HEDM reconstruction with a tighter color bar range to highlight the intragranular heterogeneity in the bulk.

The average stress component σ_{zz} from ff-HEDM and pf-HEDM is approximately 0 MPa. The spatially resolved stress maps are compared for ff-HEDM versus pf-HEDM in Fig. 7. Figure 7(a) shows the local intragranular stresses resulting from the pf-HEDM analysis, which reveals the heterogeneous stress distribution across the sample as well as across each individual grain and grain boundary.

To compare the pf-HEDM results shown in Fig. 7(a) with that of the conventional HEDM analysis, the ff-HEDM measurements of elastic strain and the nf-HEDM measurements of spatially resolved orientation were merged. Two criteria were used to connect the nf-HEDM indexed grains to the ff-HEDM indexed grains: (1) Center of the grain position within 50 microns in the Euclidean distance in the $x_L - y_L$ plane; (2) Misorientation angle within $\pm 5°$. The results are shown in Fig. 7(b). As was observed for the elastic strains in Fig. 5, the grain-averaged stress values obtained via conventional HEDM match the nominal values obtained via pf-HEDM, and the pf-HEDM results provide additional information about the intragranular stress variations inside the grains.

To highlight the importance of resolving intragranular stresses, Fig. 7(c) compares the ff-HEDM versus pf-HEDM stress values along a dotted line across the sample. The vertical dotted lines indicate where grain boundaries exist, so that the spaces between the vertical lines corresponds to individual grains. The blue horizontal lines represent the stress value converted from the ff-HEDM results, and the red scatter points represent the intragranular stress values converted from the pf-HEDM results. This comparison shows that, for some grains, the deviation between local and average stress values is small (e.g., for the grain located between $x = 410$ and 550 µm). However, for other grains, deviation between local

and average stress values can be significant (e.g., for the grains located between $x = 110$ and 160 µm, and between $x = 729$ and 780 µm). Figure 7(d) highlights the stress heterogeneity across one grain measured with pf-HEDM. Across this grain, the stress changes from -68 MPa at the bottom left region to 18 MPa at the top right region.

Furthermore, the stress discontinuity can be directly observed across each grain boundary as well as twin boundaries where present. Figure 7(a) shows many localized regions of high stress, i.e., stress concentrations, and stress gradients at and across grain boundaries. Figure 7(e–g) shows the ff-HEDM versus pf-HEDM stress values across the grain boundary between the grains labeled G2 and G3. These two grains have disparate maximum Schmid factors for plastic slip of 0.02 and 0.42, respectively. This grain pair is surrounded by grains with heterogeneous stress state, with a tensile stress as high as 40 MPa near the pair's grain boundaries (see Fig. 7(g)). Figure 7(h–j) show a boundary that can be identified as a $\{10\ \bar{1}\ 2\} < \bar{1}011>$ extension twin boundary. Although the average stress between the two grains is within 10 MPa, a sharp gradient of roughly 50 MPa can be observed across the twinning boundary labeled TB (see Fig. 7(j)).

Conclusion

The local, intragranular crystallographic orientation and elastic strain were mapped across a bulk plastically deformed CP α-Ti specimen using pf-HEDM. A novel pf-HEDM reconstruction algorithm based on the MIDAS software package is demonstrated. Compared with conventional ff-HEDM and nf-HEDM, the pf-HEDM reconstruction displays higher reconstruction confidence, especially at the grain boundary region, with significantly improved spatial
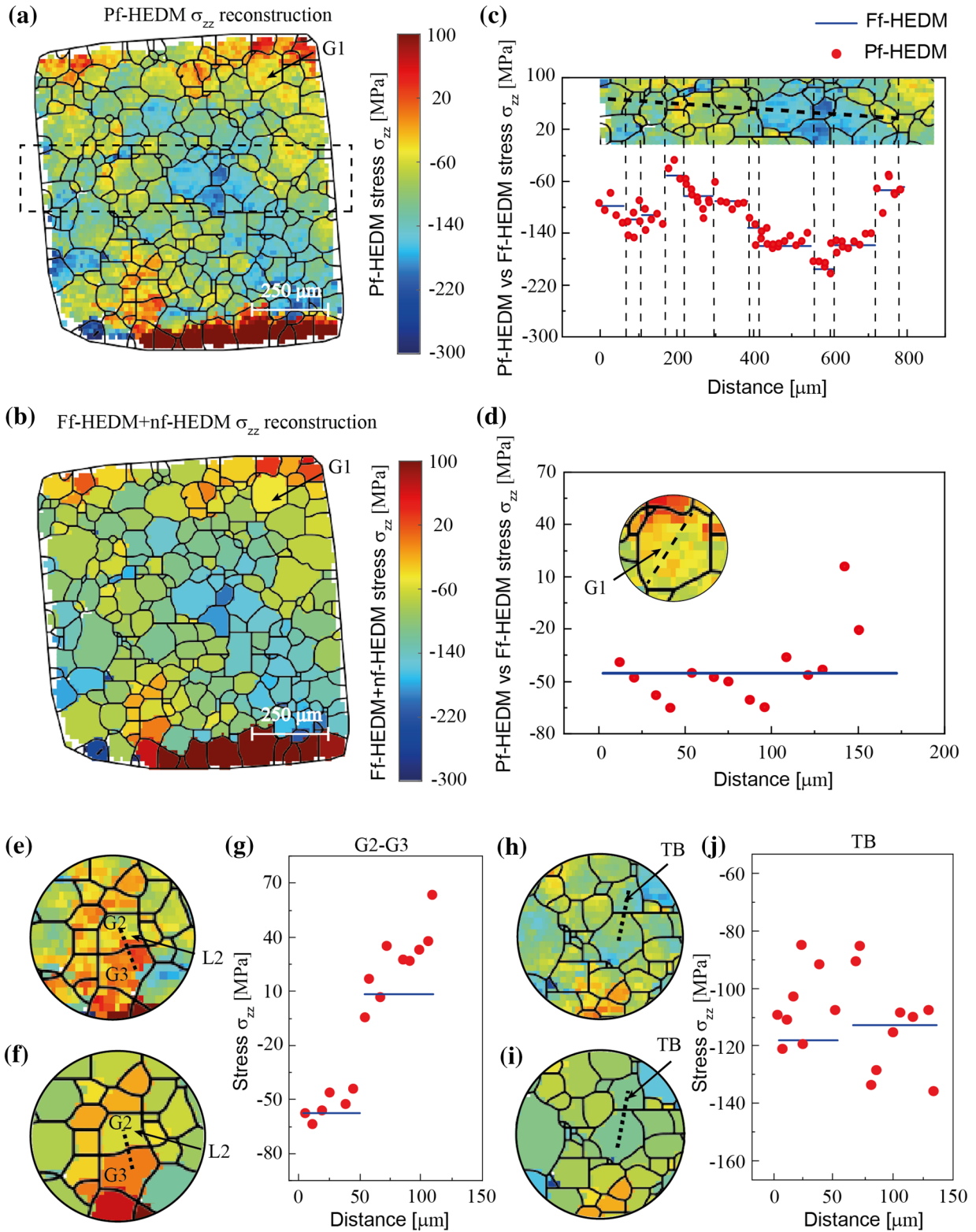
Figure 7: Ff-HEDM + nf-HEDM versus pf-HEDM comparison: (a) pf-HEDM reconstruction showing intragranular stresses in the loading direction σ_{zz}. (b) Conventional ff-HEDM + nf-HEDM reconstruction showing grain-averaged stresses in the loading direction σ_{zz} (stresses measured using ff-HEDM, spatially resolved orientation map measured using nf-HEDM). (c) Comparison of ff-HEDM versus pf-HEDM stress values along a dotted line across the sample. (d) Comparison of ff-HEDM versus pf-HEDM stress values along a dotted line across one grain labeled G1. (e, f, g) Comparison of ff-HEDM (f) versus pf-HEDM (e) stress values across a grain boundary between the grains labeled G2 and G3. (h, i, j) Comparison of ff-HEDM (i) versus pf-HEDM (h) stress values across an extension twin boundary.
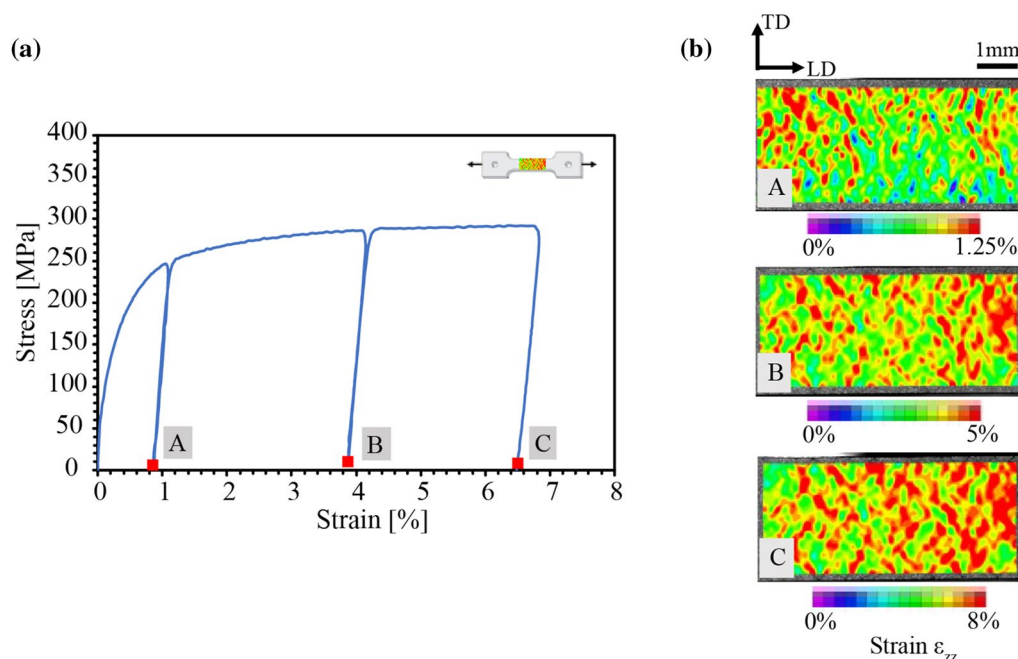
Figure 8: Macroscopic stress–strain data from tension experiment and digital image correlation images (DIC) for pure Ti specimen (a) Uniaxial tension loading curve with total displacement 0.9 mm control under strain rate of 0.1 mm/min. The yield strength is around 210 MPa. (b) DIC results in the loading direction at residual strain values of 0.85%, 3.88%, and 6.48%.

resolution. Pf-HEDM reconstruction results match well with that of conventional ff-HEDM and nf-HEDM, while the pf-HEDM results reveal the significant intragranular stress variations within individual grains and across grain boundaries. The comparison shows that the local stresses can deviate significantly from the grain-averaged stress values measured using ff-HEDM, with some stress values ranging from compressive to tensile within a single grain. We also observe a number of local, intragranular stress concentrations, including a stress concentration across a grain boundary between a grain pair with disparately low and high Schmid factors. And we also observe a number of large stress gradients, including a residual stress gradient across an extension twin boundary.

This work demonstrates the importance of developing techniques that can be used to measure local, intragranular stress concentrations and gradients such as pf-HEDM. Current mesoscale phase field and crystal plasticity simulations have evolved to the point where it is now computationally feasible to model the local stress state evolution inside a known 3D microstructure [5, 38, 39, 38–39], yet many such models still have difficulty capturing the local micromechanical evolution when significant plastic deformation has occurred. The measurement of intragranular orientation and stress evolution using pf-HEDM will significantly help inform and validate these models. These efforts will facilitate the materials science and mechanics communities' ability to predict fundamental material

and micromechanical phenomena such as plastic deformation, crack initiation, and fracture. Near-term future work includes in situ pf-HEDM measurements to characterize slip and deformation twinning events from embryo, efforts which will be aided by increasingly higher spatial resolutions enabled by beamline and synchrotron upgrades at the APS and elsewhere.

Experimental and materials

A dog bone-shaped CP α-Ti sample with a cross-section area of 2.97×1.02 mm^2 was cut out from a 99.99% Ti sputtering target (Kurt J. Lesker Company) via electrical discharge machining (EDM). The sample was encapsulated in a quartz tube with residual argon pressure of < 50 mTorr and subjected to a heat treatment at 815 °C for 4 h then air quenched. A thin non-flaky uniform oxide layer formed on the surface and revealed the underlying equiaxed grain structure of 65 μm. One side of the sample surface was hand-grinded and mechanically polished, starting with 320 grit SiC abrasive paper and eventually, 1 μm suspended alumina slurry until a mirror surface was achieved. Then 600-grit SiC particles were painted on the polished surface for digital image correlation (DIC) analysis. The Ti sample was continuously loaded in uniaxial tension at a constant crosshead displacement velocity of 0.1 mm/min using an Instron hydraulic load frame as shown in Fig. 8(a). The experiment was stopped at a final macroscopic displacement of 0.9 mm. The macroscopic stress was calculated using output from a load cell placed at the

top of the sample. An IMI-Tech 1200FT optical camera was used to collect images of the speckled surface every 2 s with 1200×1600 pixels resolution corresponding to 3.9 μm/pixel. VIC-2D from correlated solutions was used to calculate the macroscopic strains. Figure 8(b) shows the spatial distribution of the strains along loading direction at residual strain values of 0.85%, 3.88%, and 6.48%. It was clear that the strain distribution was heterogeneous and accumulates in localized regions of the sample. After loading, a $1 \times 1 \times 5$ mm^3 sample was EDM'd from the gage section with the long 5 mm axis aligned with the loading direction. The polished surface was preserved to locate and orient the HEDM scans. This plastically deformed sample (Point C) was used for the HEDM experiment.

Acknowledgments

Author contributions

A.B. conceived of and designed the experiment. W.L., A.B., H.S., and P.K. performed the ff-HEDM, nf-HEDM, and pf-HEDM experiments. S.R. and H.S. (Sehitoglu) performed the sample preparation and loading experiment. H.S. (Sharma) and W.L. analyzed the data and performed the reconstructions. W.L. wrote the manuscript. All authors provided guidance and comments on the manuscript.

Funding

Declarations

Open Access

References

1. L. Wang, M. Li, J. Almer, T. Bieler, R. Barabash, Front Mater. Sci. **7**, 156–169 (2013)

2. R. Pokharel, J. Lind, A.K. Kanjarla, R.A. Lebensohn, S.F. Li, P. Kenesei, R.M. Suter, A.D. Rollett, Annu Rev Condens Matter Phys. **5**, 317–346 (2014)

3. M.P. Miller, P.R. Dawson, Curr. Opin. Solid State Mater. Sci. **18**, 286–299 (2014)

4. J.C. Schuren, P.A. Shade, J.V. Bernier, S.F. Li, B. Blank, J. Lind, P. Kenesei, U. Lienert, R.M. Suter, T.J. Turner, D.M. Dimiduk, J. Almer, Curr. Opin. Solid State Mater. Sci. **19**, 235–244 (2015)

5. P.A. Shade, W.D. Musinski, M. Obstalecki, D.C. Pagan, A.J. Beaudoin, J.V. Bernier, T.J. Turner, Curr. Opin. Solid State Mater. Sci. **23**, 100763 (2019)

6. J.V. Bernier, R.M. Suter, A.D. Rollett, J.D. Almer, Annu. Rev. Mater. Res. **50**, 395–436 (2020)

7. H.F. Poulsen, Curr Opin Solid State Mater Sci (2020). https://doi.org/10.1016/j.cossms.2020.100820

8. D.C. Pagan, M.P. Miller, J. Appl. Crystallogr. **47**, 887–898 (2014)

9. M. Obstalecki, S.L. Wong, P.R. Dawson, M.P. Miller, Acta Mater. **75**, 259–272 (2014)

10. J. Oddershede, J.P. Wright, A. Beaudoin, G. Winther, Acta Mater. **85**, 301–313 (2015)

11. D.C. Pagan, P.A. Shade, N.R. Barton, J.S. Park, P. Kenesei, D.B. Menasche, J.V. Bernier, Acta Mater. **128**, 406–417 (2017)

12. D.C. Pagan, J.V. Bernier, D. Dale, J.Y.P. Ko, T.J. Turner, B. Blank, P.A. Shade, Scripta Mater. **142**, 96–100 (2018)

13. K. Chatterjee, A.J. Beaudoin, D.C. Pagan, P.A. Shade, H.T. Philipp, M.W. Tate, S.M. Gruner, P. Kenesei, J.S. Park, Struct Dyn. **6**, 014501 (2019)

14. C.A. Stein, A. Cerrone, T. Ozturk, S. Lee, P. Kenesei, H. Tucker, R. Pokharel, J. Lind, C. Hefferan, R.M. Suter, A.R. Ingraffea, A.D. Rollett, Curr. Opin. Solid State Mater. Sci. **18**, 244–252 (2014)

15. A.D. Spear, S.F. Li, J.F. Lind, R.M. Suter, A.R. Ingraffea, Acta Mater. **76**, 413–424 (2014)

16. D. Naragani, M.D. Sangid, P.A. Shade, J.C. Schuren, H. Sharma, J.S. Park, P. Kenesei, J.V. Bernier, T.J. Turner, I. Parr, Acta Mater. **137**, 71–84 (2017)

17. A.D. Murphy-Leonard, D.C. Pagan, A. Beaudoin, M.P. Miller, J.E. Allison, Int. J. Fatigue **125**, 314–323 (2019)

18. S. Gustafson, W. Ludwig, P. Shade, D. Naragani, D. Pagan, P. Cook, C. Yildirim, C. Detlefs, M.D. Sangid, Nat Commun. **11**, 3189 (2020)

19. J. Oddershede, B. Camin, S. Schmidt, L.P. Mikkelsen, H.O. Sørensen, U. Lienert, H.F. Poulsen, W. Reimers, Acta Mater. **60**, 3570–3580 (2012)

20. P. Ravi, D. Naragani, P. Kenesei, J.S. Park, M.D. Sangid, Acta Mater. **205**, 116564 (2021)

21. V. Prithivirajan, P. Ravi, D. Naragani, M.D. Sangid, Mater. Des. **197**, 109216 (2021)

22. C. Lou, X. Zhang, Y. Ren, Mater. Charact. **107**, 249–254 (2015)

23. M.R. Barnett, Z. Keshavarz, A.G. Beer, X. Ma, Acta Mater. **56**, 5–15 (2008)

24. I. Beyerlein, R. McCabe, C. Tomé, J. Mech. Phys. Solids **59**, 988–1003 (2011)

25. I. Beyerlein, C. Tomé, Proc. Royal Soc. A: Math. Phys. Eng. Sci. **466**, 2517–2544 (2010)

26. I. Beyerlein, L. Capolungo, P. Marshall, R. McCabe, C. Tomé, Phil. Mag. **90**, 2161–2190 (2010)

27. J. Lind, S. Li, R. Pokharel, U. Lienert, A. Rollett, R. Suter, Acta Mater. **76**, 213–220 (2014)

28. A.K. Kanjarla, I.J. Beyerlein, R.A. Lebensohn, C. Tomé, Mater Sci Forum **702**, 265–268 (2011)

29. C. Barrett, H. El Kadiri, M. Tschopp, J. Mech. Phys. Solids **60**, 2084–2099 (2012)

30. L. Nervo, A. King, A. Fitzner, W. Ludwig, M. Preuss, Acta Mater. **105**, 417–428 (2016)

31. A. Akhtar, Metall. Trans. A **6**, 1105 (1975)

32. X. Tan, H. Gu, C. Laird, N.D.H. Munroe, Metall. and Mater. Trans. A. **29**, 507–512 (1998)

33. K. Hagihara, T. Nakano, Y. Umakoshi, MRS Proc. (2011). https://doi.org/10.1557/PROC-646-N5.23.1

34. L. Xiao, Y. Umakoshi, Mater. Sci. Eng., A **339**, 63–72 (2003)

35. S. Xu, M. Gong, C. Schuman, J.S. Lecomte, X. Xie, J. Wang, Acta Mater. **132**, 57–68 (2017)

36. Z.Z. Shi, Y. Zhang, F. Wagner, P.A. Juan, S. Berbenni, L. Capolungo, J.S. Lecomte, T. Richeton, Acta Mater. **83**, 17–28 (2015)

37. T.R. Bieler, L. Wang, A.J. Beaudoin, P. Kenesei, U. Lienert, Metall Mat Trans A. **45**, 109–122 (2013)

38. H. Abdolvand, M. Majkut, J. Oddershede, J.P. Wright, M.R. Daymond, Acta Mater. **93**, 246–255 (2015)

39. H. Abdolvand, M. Majkut, J. Oddershede, J.P. Wright, M.R. Daymond, Acta Mater. **93**, 235–245 (2015)

40. L. Capolungo, P. Marshall, R. McCabe, I. Beyerlein, C. Tomé, Acta Mater. **57**, 6047–6056 (2009)

41. M.A. Kumar, M. Wroński, R.J. McCabe, L. Capolungo, K. Wierzbanowski, C.N. Tomé, Acta Mater. **148**, 123–132 (2018)

42. J.D. Carroll, W. Abuzaid, J. Lambros, H. Sehitoglu, Int. J. Fatigue **57**, 140–150 (2013)

43. J.D. Carroll, W.Z. Abuzaid, J. Lambros, H. Sehitoglu, Int J Fract. **180**, 223–241 (2013)

44. M.D. Sangid, Int. J. Fatigue **57**, 58–72 (2013)

45. W.Z. Abuzaid, M.D. Sangid, J.D. Carroll, H. Sehitoglu, J. Lambros, J. Mech. Phys. Solids **60**, 1201–1220 (2012)

46. C. Blochwitz, W. Tirschler, Cryst. Res. Technol. **40**, 32–41 (2005)

47. M.D. Sangid, H.J. Maier, H. Sehitoglu, Int. J. Plast **27**, 801–821 (2011)

48. D. Ando, J. Koike, Y. Sutou, Mater. Sci. Eng., A **600**, 145–152 (2014)

49. D.A. Basha, H. Somekawa, A. Singh, Scripta Mater. **142**, 50–54 (2018)

50. M.T. Andani, A. Lakshmanan, M. Karamooz-Ravari, V. Sundararaghavan, J. Allison, A. Misra, Sci Rep. **10**, 3084 (2020)

51. T. Benjamin Britton, A.J. Wilkinson, Acta Mater. **60**, 5773–5782 (2012)

52. Y. Guo, T.B. Britton, A.J. Wilkinson, Acta Mater. **76**, 1–12 (2014)

53. Y. Guo, D.M. Collins, E. Tarleton, F. Hofmann, J. Tischler, W. Liu, R. Xu, A.J. Wilkinson, T.B. Britton, Acta Mater. **96**, 229–236 (2015)

54. L. Balogh, S.R. Niezgoda, A.K. Kanjarla, D.W. Brown, B. Clausen, W. Liu, C.N. Tomé, Acta Mater. **61**, 3612–3620 (2013)

55. M. Arul Kumar, B. Clausen, L. Capolungo, R.J. McCabe, W. Liu, J.Z. Tischler, C.N. Tomé, Nat Commun. **9**, 4761 (2018)

56. N. Mavrikakis, C. Detlefs, P.K. Cook, M. Kutsal, A.P.C. Campos, M. Gauvin, P.R. Calvillo, W. Saikaly, R. Hubert, H.F. Poulsen, A. Vaugeois, H. Zapolsky, D. Mangelinck, M. Dumont, C. Yildirim, Acta Mater. **174**, 92–104 (2019)

57. U. Lienert, M. C. Brandes, J. V. Bernier, M. J. Mills, M. P. Miller, S. F. Li, C. M. Hefferan, J. Lind, R. M. Suter, Proceedings of the 31st. Risø International Symposium on Materials Science, Risø National Laboratory, Roskilde, Denmark (2010). https://apps.dtic.mil/sti/citations/ADA543233.

58. H.F. Poulsen, *Three-dimensional X-ray diffraction microscopy: mapping polycrystals and their dynamics* (Springer, Berlin, 2004)

59. H.F. Poulsen, Crystallogr. Rev. **10**, 29–43 (2004)

60. H.F. Poulsen, J Appl Cryst. **45**, 1084–1097 (2012)

61. J.V. Bernier, N.R. Barton, U. Lienert, M.P. Miller, J. Strain Anal. Eng. Des. **46**, 527–547 (2011)

62. J.S. Park, X. Zhang, P. Kenesei, S.L. Wong, M. Li, J. Almer, Microscopy Today. **25**, 36–45 (2017)

63. M.B. Dixit, B.S. Vishugopi, W. Zaman, P. Kenesei, J.S. Park, J. Almer, P.P. Mukherjee, K.B. Hatzell, Nat. Mater. **21**, 1298–1305 (2022)

64. R.M. Suter, D. Hennessy, C. Xiao, U. Lienert, Rev. Sci. Instrum. **77**, 123905 (2006)

65. S.F. Li, R.M. Suter, J Appl Cryst. **46**, 512–524 (2013)

66. P. Reischig, W. Ludwig, Curr. Opin. Solid State Mater. Sci. (2020). https://doi.org/10.1016/j.cossms.2020.100851

67. Y.F. Shen, H. Liu, R.M. Suter, Curr. Opin. Solid State Mater. Sci. **24**, 100852 (2020)

68. J.S. Park, H. Sharma, P. Kenesei, J Synchrotron Rad. **28**, 1786–1800 (2021)

69. S.F. Li, J. Lind, C.M. Hefferan, R. Pokharel, U. Lienert, A.D. Rollett, R.M. Suter, J. Appl. Crystallogr. **45**, 1098–1108 (2012)

70. L. Renversade, R. Quey, W. Ludwig, D. Menasche, S. Maddali, R.M. Suter, A. Borbély, IUCrJ. **3**, 32–42 (2016)

71. D.P. Naragani, P.A. Shade, P. Kenesei, H. Sharma, M.D. Sangid, Acta Mater. **179**, 342–359 (2019)

72. M.D. Sangid, J. Rotella, D. Naragani, J.S. Park, P. Kenesei, P.A. Shade, Acta Mater. **201**, 36–54 (2020)

73. A. Yau, W. Cha, M.W. Kanan, G.B. Stephenson, A. Ulvestad, Science **356**, 739–742 (2017)

74. A. Ulvestad, Y. Nashed, G. Beutier, M. Verdier, S.O. Hruszkew-ycz, M. Dupraz, Sci Rep. **7**, 9920 (2017)

75. M.J. Cherukara, R. Pokharel, T.S. O'Leary, J.K. Baldwin, E. Maxey, W. Cha, J. Maser, R.J. Harder, S.J. Fensin, R.L. Sandberg, Nat Commun. **9**, 3776 (2018)

76. N. Li, M. Dupraz, L. Wu, S.J. Leake, A. Resta, J. Carnis, S. Labat, E. Almog, E. Rabkin, V. Favre-Nicolin, F.E. Picca, F. Berenguer, R. van de Poll, J.P. Hofmann, A. Vlad, O. Thomas, Y. Garreau, A. Coati, M.I. Richard, Sci Rep. **10**, 12760 (2020)

77. H. Simons, A. King, W. Ludwig, C. Detlefs, W. Pantleon, S. Schmidt, F. Stöhr, I. Snigireva, A. Snigirev, H.F. Poulsen, Nat Commun. **6**, 6098 (2015)

78. H. Simons, A.C. Jakobsen, S.R. Ahl, C. Detlefs, H.F. Poulsen, MRS Bull. **41**, 454–459 (2016)

79. A.C. Jakobsen, H. Simons, W. Ludwig, C. Yildirim, H. Leemreize, L. Porz, C. Detlefs, H.F. Poulsen, J Appl Cryst. **52**, 122–132 (2019)

80. A. Bucsek, H. Seiner, H. Simons, C. Yildirim, P. Cook, Y. Chumlyakov, C. Detlefs, A.P. Stebner, Acta Mater. **179**, 273–286 (2019)

81. B.C. Larson, W. Yang, G.E. Ice, J.D. Budai, J.Z. Tischler, Nature **415**, 887–890 (2002)

82. L.E. Levine, B.C. Larson, W. Yang, M.E. Kassner, J.Z. Tischler, M.A. Delos-Reyes, R.J. Fields, W. Liu, Nature Mater. **5**, 619–622 (2006)

83. G.E. Ice, J.D. Budai, J.W.L. Pang, Science **334**, 1234–1239 (2011)

84. Y. Hayashi, D. Setoyama, Y. Hirose, T. Yoshida, H. Kimura, Science **366**, 1492–1496 (2019)

85. J. Hektor, S.A. Hall, N.A. Henningsson, J. Engqvist, M. Ristin-maa, F. Lenrick, J.P. Wright, Materials. **12**, 446 (2019)

86. N.A. Henningsson, S.A. Hall, J.P. Wright, J. Hektor, J. Appl. Crystallogr. **53**, 314–325 (2020)

87. Y. Hayashi, Y. Hirose, D. Setoyama, Mater. Sci. Forum **777**, 118–123 (2014)

88. Y. Hayashi, Y. Hirose, Y. Seno, J. Appl. Crystallogr. **48**, 1094–1101 (2015)

89. Y. Hayashi, Y. Hirose, Y. Seno, AIP Conf. Proc. **1741**, 050024 (2016)

90. A. Henningsson, J. Hendriks, J Appl Crystallogr. **54**, 1057–1070 (2021)

91. E.M. Lauridsen, S. Schmidt, R.M. Suter, H.F. Poulsen, J Appl Cryst. **34**, 744–750 (2001)

92. W. Ludwig, P. Reischig, A. King, M. Herbig, E.M. Lauridsen, G. Johnson, T.J. Marrow, J.Y. Buffière, Rev. Sci. Instrum. **80**, 033905 (2009)

93. M. Moscicki, P. Kenesei, J. Wright, H. Pinto, T. Lippmann, A. Borbély, A.R. Pyzalla, Mater. Sci. Eng., A **524**, 64–68 (2009)

94. H. Sharma, R.M. Huizenga, S.E. Offerman, J. Appl. Crystallogr. **45**, 693–704 (2012)

95. H. Sharma, R.M. Huizenga, S.E. Offerman, J. Appl. Crystallogr. **45**, 705–718 (2012)

96. H.F. Poulsen, S. Garbe, T. Lorentzen, D. Juul Jensen, F.W. Poulsen, N.H. Andersen, T. Frello, R. Feidenhans'l, H. Graaf-sma, J Synchrotron Rad. **4**, 147–154 (1997)

97. S.F. Nielsen, A. Wolf, H.F. Poulsen, M. Ohler, U. Lienert, R.A. Owen, J Synchrotron Rad. **7**, 103–109 (2000)

98. H.F. Poulsen, S. Schmidt, J Appl Cryst. **36**, 319–325 (2003)

99. D. P. Kingma, J. Ba, Adam: A method for stochastic optimization (2017), (available at http://arxiv.org/abs/1412.6980).

100. S.D. Shastri, K. Fezzaa, A. Mashayekhi, W.K. Lee, P.B. Fernan-dez, P.L. Lee, J Synchrotron Rad. **9**, 317–322 (2002)

101. J.H. Lee, C.C. Aydıner, J. Almer, J. Bernier, K.W. Chapman, P.J. Chupas, D. Haeffner, K. Kump, P.L. Lee, U. Lienert, A. Miceli, G. Vera, J Synchrotron Rad. **15**, 477–488 (2008)

102. S.D. Shastri, P. Kenesei, A. Mashayekhi, P.A. Shade, J Synchro-tron Rad. **27**, 590–598 (2020)

103. J.V. Bernier, N.R. Barton, U. Lienert, M.P. Miller, J Strain Anal Eng Design **2011**, 0309324711405761 (2011)

104. S.L. Wong, J.S. Park, M.P. Miller, P.R. Dawson, Comput. Mater. Sci. **77**, 456–466 (2013)

105. F. Bachmann, R. Hielscher, H. Schaeben, Solid State Phenom. **160**, 63–68 (2010)

106. D. Tromans, Int. J. Res. Rev. Appl. Sci. **6**, 462–483 (2011)

107. D. Naragani, P. Shade, W. Musinski, D. Boyce, M. Obstalecki, D. Pagan, J. Bernier, A. Beaudoin, Mater. Des. **210**, 110053 (2021)

108. H.M. Paranjape, P.P. Paul, H. Sharma, P. Kenesei, J.S. Park, T.W. Duerig, L.C. Brinson, A.P. Stebner, J. Mech. Phys. Solids **102**, 46–66 (2017)

109. H.M. Paranjape, P.P. Paul, B. Amin-Ahmadi, H. Sharma, D. Dale, J.Y.P. Ko, Y.I. Chumlyakov, L.C. Brinson, A.P. Stebner, Acta Mater. **144**, 748–757 (2018)

Publisher's Note Springer Nature remains neutral with regard to jurisdictional claims in published maps and institutional affiliations.